Lithos 105 (2008) 98–110

Contents lists available at ScienceDirect

Lithos

journal homepage: www.elsevier.com/locate/lithos

Oxidation state of Paleozoic subcontinental lithospheric mantle below the Pali Aike volcanic field in southernmost Patagonia

Jian Wang [a,b,*], Keiko H. Hattori [a], Jianping Li [a], Charles R. Stern [c]

[a] Department of Earth Sciences, University of Ottawa, Ottawa, Ontario, Canada K1N 6N5
[b] College of Earth Sciences, Jilin University, Changchun, Jilin, 130061, China
[c] Department of Geological Sciences, University of Colorado, Boulder, CO 80309-0399, USA

ARTICLE INFO

Article history:
Received 20 October 2007
Received in revised form
Accepted 20 February 2008
Available online 5 March 2008

Keywords:
Southern Patagonia
Accretion
Slab window
Peridotite xenoliths
Mantle oxidation condition
Mantle metasomatism

ABSTRACT

Mantle xenoliths in the Quaternary Pali Aike alkaline basalts of southernmost Patagonia include lherzolites and harzburgites with and without garnet. The values of fO_2 for all xenoliths range from 0.33 logarithmic unit below the fayalite–magnetite–quartz buffer (FMQ−0.33) to FMQ+0.75, which overlap those for abyssal peridotites. The fO_2 data, together with the bulk rock and mineral compositions, suggest that the subcontinental lithospheric mantle (SCLM) below Pali Aike formed through the accretion of oceanic lithosphere. The oceanic accretion likely occurred in mid to late Paleozoic time when the southern Patagonian terrane formed along the southwest margin of Gondwana. Relict spinel inclusions in garnet suggest that garnet-facies peridotites formed from spinel-facies peridotites most likely in response to pressure increase during the accretion. Comparable fO_2 for garnet- and spinel-facies peridotites suggests that this spinel-garnet transformation was not accompanied by changes in fO_2.

Metasomatism by asthenosphere-derived melt through a slab window resulted in the formation of Ti-bearing minerals, and lowering of Mg and enrichment of Ti in bulk rocks and minerals. The replacement of olivine by orthopyroxene formed orthopyroxenites in extreme cases. No significant change in fO_2 is associated with this metasomatism since similar oxidation state is observed between un-metasomatized (FMQ−0.23 to +0.48) and metasomatized (FMQ−0.33 to +0.75) samples. This is explained by the fO_2 of the asthenospheric melt (~FMQ−0.50) similar to the SCLM prior to the metasomatism.

1. Introduction

Mantle oxidation state is important in controlling the composition and nature of partial melt. For example, diamond forms in reduced subcontinental lithospheric mantle (SCLM) beneath old cratons and remains stable during transportation to surface by kimberlites (McCammon et al., 2001). In contrast, oxidized sub-arc mantle is conducive to forming high sulfur magmas (DeHoog et al., 2004) and large Au and Cu deposits because metals can be effectively partitioned to partial melt under oxidized conditions (Hattori and Keith, 2001; Mungall, 2002). Furthermore, the amount of V in partial melt may be affected by the oxidation state of the mantle source (Canil, 1997, 2002).

A significant variation is observed in fO_2 in lithospheric upper mantle, but its causes are still not well understood. Partial melting is generally considered to result in low fO_2 in the residual mantle as Fe^{3+} is preferentially incorporated in melt (e.g., Canil et al., 1994). This is supported by low fO_2 in refractory peridotites beneath ancient cratons that show high Cr# (atomic ratio of Cr/[Cr+Al]) in spinel (e.g., Woodland and Koch, 2003). In contrast, a positive correlation between fO_2 and Cr# in spinel is observed in sub-arc mantle peridotites and this is explained by the infiltration of oxidizing fluids from slabs (e.g., Ballhaus, 1993; Parkinson and Arculus, 1999).

Previous studies on the oxidation state of SCLM focused on those underlying Archean continents, such as Kaapvaal craton (South Africa; Daniels and Gurney, 1991; McCammon et al., 2001; Woodland and Koch, 2003) and Slave province of the Canadian Shield (e.g., McCammon and Kopylova, 2004). Studies on oxidation state of Phanerozoic SCLM have thus far not been reported. Southern Patagonia in the southernmost part of South America is considered to have docked with Gondwana to form the South American continent in the Paleozoic (e.g., Rapalini, 2005; Pankhurst et al., 2006). Subsequently, the SCLM below the Patagonian terrane underwent metasomatism by melt derived from the underlying asthenosphere (Kempton et al., 1999a,b; Stern et al., 1999). Therefore, mantle xenoliths from Patagonian basalts contain information relevant to the formation and later modification of the Phanerozoic SCLM of the Patagonian terrane. This paper reports the bulk rock compositions, mineral chemistry, and the oxidation conditions of representative

* Corresponding author. College of Earth Sciences, Jilin University, Changchun, Jilin, 130061, China.
E-mail address: jian.wang1205@gmail.com (J. Wang).

0024-4937/$ – see front matter © 2008 Elsevier B.V. All rights reserved.
doi:10.1016/j.lithos.2008.02.009

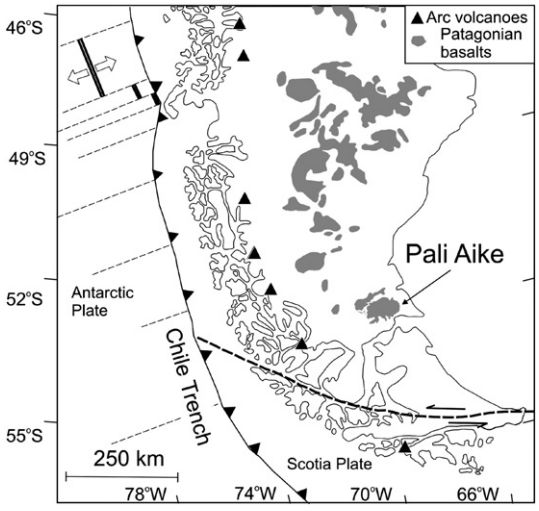

Fig. 1. The location of the study area and the distribution of the alkaline basalt fields of Pali Aike, and other late Cenozoic basalts of Patagonian plateau. Also shown are volcanoes of the Andean Austral Zone (AVZ) (modified after Wang et al., 2007).

mantle peridotite xenoliths from the Quaternary Pali Aike basalts, southernmost Patagonia (Fig. 1), and discusses the origin and evolution of this relatively young SCLM.

2. Tectonic setting

There is considerable debate regarding the origin and tectonic evolution of the southern portion of the Patagonian terrane, and its relations with Gondwana (e.g., Ramos, 1986; Von Gonsen, 2002; Pankhurst et al., 2003; Rapalini, 2005; Pankhurst et al., 2006). Pali Aike is located south of the Deseado Massif, the main part of southern Patagonia. The Deseado Massif consists in part of metasedimentary rocks of Neoproterozoic age (580 Ma; Pankhurst et al., 2003, 2006), which were rifted from Gondwana in the late Proterozoic to early Cambrian. It was later united again with northern Patagonia through the subduction of an intervening oceanic lithosphere during the late Paleozoic. Metamorphosed basement from Tierra del Fuego, ~100 km south of Pali Aike, has been dated at 529 Ma by U–Pb in zircons (Söllner et al., 2000). Thus the basement below Pali Aike may be either part of this Deseado Massif, or may have been accreted to the Deseado Massif in Paleozoic time. Either way, the basement and SCLM below the Pali Aike area is clearly not Archean or early Proterozoic, but relatively young accretionary lithosphere of Phanerozoic age.

During the late Jurassic break-up of Gondwana, voluminous rhyolitic volcanism formed the Chon Aike Formation in southern Patagonia (Bruhn et al., 1978; Kay et al., 1989). Since the late Jurassic or early Cretaceous, the area has been dominated by subsidence and sedimentation, forming the Magallanes basin, whereas the eastward subduction of oceanic plates beneath the western margin of South America produced the Andes on the western margin of the South America.

The Chile ridge between the Nazca and Antarctic Plates collided with the trench near the southern tip of South America at ~14–15 Ma, forming a triple junction (Cande and Leslie, 1986) which has since migrated northward to its present position at 46.5° S (Fig. 1). Ridge subduction was responsible for Neogene uplift of the southernmost sector of the Andes, and formation of the Patagonian fold-thrust belt (Ramos, 1989; Haschke et al., 2006). Ridge subduction also resulted in upwelling of underlying asthenospheric mantle through a slab window, which produced extensive alkali plateau basaltic rocks in southern Patagonia (Gorring et al., 1997; D'Orazio et al., 2000). These plateau basalts range in age from late Miocene to Recent and systematically young to the northeast following the track of the subducted ridge. The Pali Aike volcanic field, which covers 4500 km^2, is the southernmost among the Patagonian plateau basalts (Fig. 1; D'Orazio et al., 2000). The subduction of Antarctic plate, west of the subducted ridge, is producing the adakitic andesite stratovolcanoes of the Andean Austral Volcanic Zone, ~250 km west of the Pali Aike area (Fig. 1; Stern and Kilian, 1996).

3. Samples

The Pali Aike volcanic field contains lavas as well as pyroclastic rocks, including tuff breccias associated with maars as well as both spatter and scoria cones, of alkali basaltic composition. Some of the basaltic lavas and pyroclastic rocks contain peridotite and pyroxenite xenoliths (Stern et al., 1999). Mantle xenoliths used in this study were collected from a small scoria cone (samples BN and BNC; 52°02′23″ S and 70°04′08″ W) within a tuff ring around a large maar (samples BNH). These sample sites are located at the southeast end of a SE–NW trending chain of maars and cones, just north of the north branch (Brazo Norte) of the dry river (Rio Seco). Mantle xenolith samples were also collected from the maar enclosing Timone Lake (samples TM; 52°00′58″ S and 70°12′16″ W) to the northwest along this same chain. Other samples were collected from the tuff ring around Laguna Salida (now called Laguna Ana: samples LS; 52°04′30″ S and 69°47′18″ W) maar, and another tuff ring (samples PAK and PA; 52°06′06″ S and 69°43′48″ W) to the southeast along the fissure that also includes the Pali Aike cone.

We examined a total of thirty-two mantle xenoliths ranging in size from 3 to 20 cm in the longest dimension. Samples are rounded and show no evidence of weathering and serpentinization, but the rims of several samples show the evidence of interaction with host basaltic magma. These parts were removed before preparing samples for bulk rock analysis. Six samples (LS33, BN50, TM15, TM0, TM2, and LS1) were described previously by Stern et al. (1999). In this study, we have re-analyzed major element compositions for these six samples and further determined mineral compositions together with the other twenty-six new samples.

Table 1
Mantle xenoliths from the Pali Aike area, southern Patagonia

Xenolith group	Rock type	Assemblage	Samples*
Peridotites	Grt lherzolite	Ol+Opx+Cpx+Grt	**LS33**
	Grt-Spl lherzolite	Ol+Opx+Cpx+Grt+Spl	**TM0**, **TM2**, LS50, BN73, LS1, **BN32**
	Grt-Spl harzburgite	Ol+Opx+Grt+Spl±Cpx	**TM14**, **TM15**, **BN92**, **BN50**, **PAK6**, **PAHK1**, **BN45**, **BN31**
	Spl lherzolite	Ol+Opx+Cpx+Spl	**PA64**, PAK1
	Spl harzburgite	Ol+Opx+Spl±Cpx	LS5, PAK2, PAK3, 01BN, BNH11, **LS100**, **PAK5**
Pyroxenite	Grt orthopyroxenite	Opx+Grt+Ilm+Ti-Phl+Ti-Amp±Ol±Cpx	**BNH13**, **BNC2**, **BNC1**, **BN43**, **BNO5**, **BNC3**, **BNH5**, **BN46**

Abbreviations: Cpx = clinopyroxene, Grt = garnet, Ol = olivine, Opx = orthopyroxene, Spl = spinel, Ti-Phl = Ti-phlogopite, Ti-Amp = Ti-amphibole, Ilm = ilmenite.
*Bold = samples affected by cryptic metasomatism showing low Mg# and high Ti in minerals and bulk rock compositions.
*Underlined bold = modally metasomatized samples containing Ti-Amp, Ti-Phl, or Mg-Ilm.

The mantle xenoliths are divided into two types; peridotites (lherzolites and harzburgites) and pyroxenites. Their mineralogy is listed in Table 1. Peridotites are further divided into five subtypes based on the presence of garnet and/or spinel: garnet lherzolite (n=1), garnet-spinel lherzolite (n=6), spinel lherzolite (n=2), garnet-spinel harzburgite (n=8), and spinel harzburgite (n=7). Pyroxenite xenoliths are orthopyroxenites and minor websterites. This paper focuses on peridotite samples.

Garnet-bearing lherzolites consist mainly of olivine (50–70 vol.%), orthopyroxene (15–30 vol.%), clinopyroxene (5–20 vol.%), garnet (5–15 vol.%) and spinel (≤2 vol.%). They show coarse-grained (1–4 mm) equigranular to porphyroblastic textures (Fig. 2a). Garnet-spinel harzburgites show porphyroblastic to equigranular (1–4 mm) texture (Fig. 2b) and contain olivine (50–70 vol.%), orthopyroxene (25–30 vol.%), and garnet (5–10 vol.%) with minor spinel (≤2 vol.%) and clinopyroxene (≤0.5 vol.%). Garnet (1–6 mm) shows a symplectic rim (>50 μm), which consists of a mixture of fine-grained pyroxenes and spinel, that was most likely formed during the ascent of the xenoliths. Relict spinel (up to 2 mm) with reaction rims are common in garnet (Fig. 2c), suggesting that garnet is a reaction product of spinel. Spinel also forms inclusions (0.2–0.3 mm) and intergrowth with olivine and pyroxene (up to 2 mm) in garnet-bearing peridotites. Spinel peridotites show grain sizes and mineral assemblages similar to garnet-bearing peridotites.

Orthopyroxenite (n=8) occurs either as discrete xenoliths or veinlets (>5 mm) in garnet-bearing harzburgites (Fig. 2d). Discrete orthopyroxenite xenoliths commonly contain small angular dunite and/or harzburgite fragments (5–10 mm in size) with diffuse boundaries. Orthopyroxenites show equigranular and/or porphyroblastic texture with coarse garnet (up to 5 mm) and orthopyroxene (up to 4 mm). They are composed of orthopyroxene (≥85 vol.%), garnet, olivine, Ti-phlogopite, Ti-amphibole, Mg-ilmenite, and minor sulphide minerals (pentlandite and pyrrhotite), with or without minor clinopyroxene. The veinlets of orthopyroxenite contain the same mineral assemblage as orthopyroxenite xenoliths and are accompanied by halos of secondary orthopyroxene (Fig. 2d).

4. Analytical methods and calculation of fO_2

4.1. Microprobe analysis

Mineral compositions were determined using the Camebax MBX electron probe at Carleton University in Ottawa and the JEOL 8900 Super probe at McGill University in Montreal. Camebax MBX electron

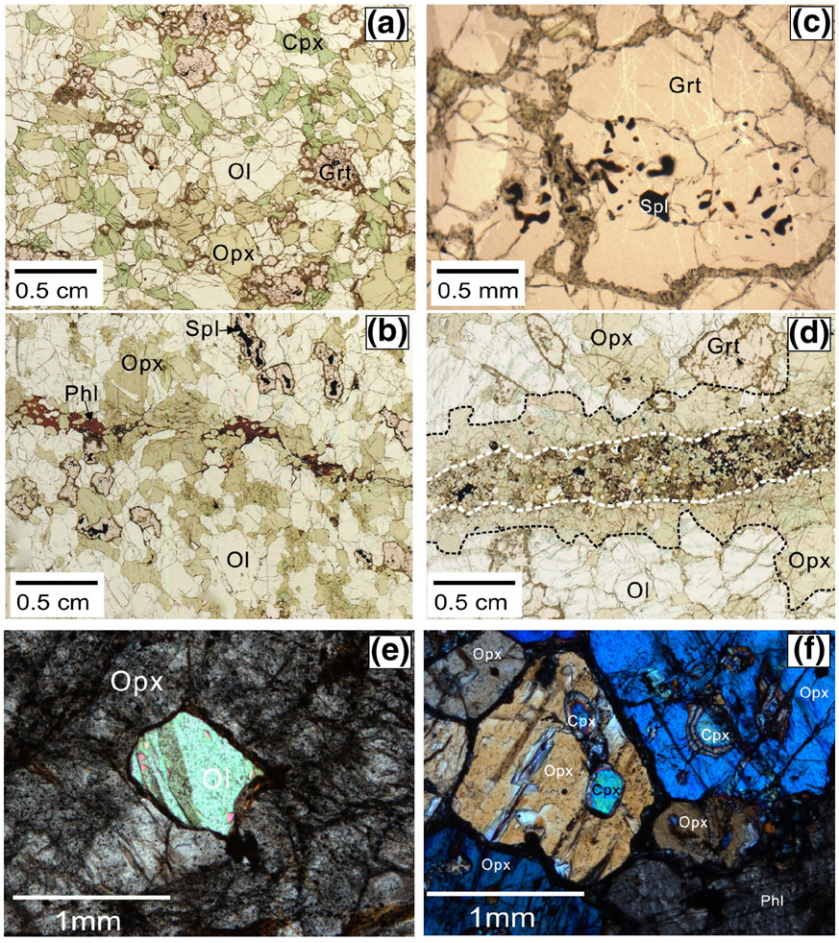

Fig. 2. (a) Photograph of a garnet-spinel lherzolite (sample TM2). (b) Photograph of a metasomatized garnet-spinel harzburgite (sample TM15). Note that discontinuous phlogopite veinlet cuts across the host harzburgite. Also shown in subpanel (b) is the relict spinel enclosed in large garnet. (c) Photomicrograph of coarse garnet enclosing relict spinel grain in garnet-spinel harzburgite (sample BN32) under plane polarized light. Note that there is a reaction rim between relict spinel and host garnet. (d) Photograph of an orthopyroxenite veinlet in garnet-spinel harzburgite (sample BN92). The veinlet (shown with white dashed lines) is accompanied by metasomatic halos (shown with black dashed lines). Red = garnet, opaque minerals = ilmenite, yellow green = orthopyroxene, and transparent = olivine. (e) Photomicrograph of orthopyroxene (Opx) enclosing a relict olivine grain in orthopyroxenite (sample BNC1). Note cloudy secondary Opx with abundant fluid inclusions. (f) Photomicrograph of secondary Opx enclosing relict clinopyroxene (Cpx) in orthopyroxenite under cross polarized light (sample BN46). Note the ~120° angle at triple junctions of grain boundaries of the secondary Opx in the upper part of the photograph. (For interpretation of the references to color in this figure legend, the reader is referred to the web version of this article.)

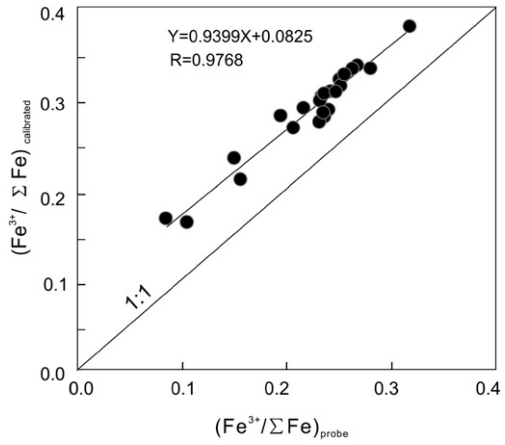

Fig. 3. Comparison between the ratios of $(Fe^{3+}/\sum Fe)_{probe}$ and $(Fe^{3+}/\sum Fe)_{calibrated}$ of spinel samples in mantle peridotites from Pali Aike. Ratios of $(Fe^{3+}/\sum Fe)_{probe}$ are calculated assuming stoichiometry of spinel compositions and each point represent an average of 5–8 grains in each sample. Calibrated ratios, $(Fe^{3+}/\sum Fe)_{calibrated}$, were obtained using four spinel standard samples (KLB8304, KLB8311, MBR8305 and KLB8316) with known Fe^{3+} contents following the method described by Wood and Virgo (1989).

probe was operated with 15 kV acceleration voltage, ~20 nA beam current, and focused beam size of <1 μm. Counting time was 20 s for all elements except 50 s for Ca in olivine. JEOL 8900 Super Probe was operated with 20 kV acceleration voltage, 20 nA beam current, and 1 μm beam size. Counting time of 30 s was used for most elements except 50 s for Ca in olivine. Cameca PAP and ZAF correction procedures were applied to raw data for Camebax MBX and JEOL 8900 probes, respectively. A suite of well characterized natural and synthetic minerals were used as standards in both probes.

4.2. Bulk rock analysis

For the bulk rock composition analysis, rims and veins were removed before grinding samples. Major and minor elements were determined using a Philips PW 2400 X-ray fluorescence spectrometer after fusing the sample powder with $LiBO_3$ at the University of Ottawa. Precision based on replicate runs of eleven samples is ±0.35% for Al_2O_3, ±0.48% for MgO, ±1.3% for Cr, and ±9.2% for Ni. The accuracy, which was monitored using references of MRG-1 and Sy-2, shows ±0.039% for Al_2O_3, 0.28% for MgO, 3.4% for Cr, and 4.0% for Ni. Accuracy is less than 1% and 10% for other major and minor elements, respectively. Loss of ignition was determined after heating samples at 1050 °C for 1.5 h.

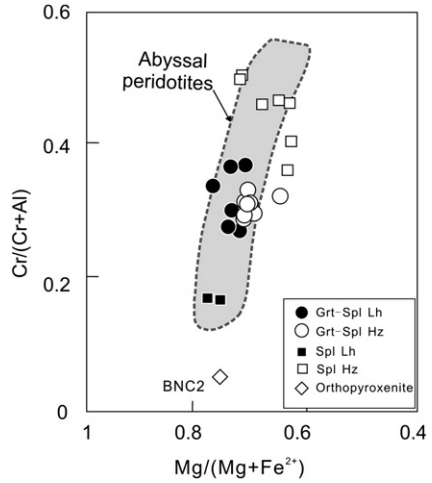

Fig. 4. Plot of Cr# vs. $Mg/(Mg+Fe^{2+})$ for spinel in peridotites from Pali Aike, compared with the data for abyssal peridotites (Dick and Bullen, 1984). Each point represents an average of 5 to 8 grains of spinel in each thin-section. Abbreviations for mineral and rock; Grt = garnet, Spl = spinel, Lh = lherzolite, Hz = harzburgite.

4.3. Calculation of fO_2

The fO_2 values are calculated using the following reaction equilibrium:

$$6Fe_2SiO_4(\text{olivine}) + O_2 \rightarrow 3Fe_2Si_2O_6(\text{orthopyroxene}) + 2Fe_3O_4(\text{spinel}) \quad (1)$$

The Fe^{3+} contents are converted to activities of Fe_3O_4 using the formula of Nell and Wood (1991):

$$\log a_{Fe_3O_4} = \log((Fe^{2+})\cdot(Fe^{3+})^2/4) + 1/T[406(Al)^2 + 653(Mg)(Al) + 299(Cr)^2 + 199(Al)(Cr) + 346(Mg)(Cr)] \quad (2)$$

where the term in parentheses refers to total atomic concentration of Mg, Fe^{2+}, Fe^{3+}, Cr and Al in spinel on a four oxygen basis.

The fO_2 is estimated relative to the FMQ buffer, as follows:

$$\log(fO_2)_{P,T} = \log(fO_2)FMQ + 220/T + 0.35-0.0369P/T-12\log X_{Fe}^{Ol}-2620(X_{Mg}^{Ol})^2/T + 3\log(X_{Fe}^{M1}\cdot X_{Fe}^{M2})^{Opx} + 2\log a_{Fe_3O_4}^{spinel} \quad (3)$$

where P is bar, T in K, X_{Fe}^{Ol} and X_{Mg}^{Ol} refer to the $Fe^{2+}/(Fe^{2+}+Mg)$ and $Mg/(Fe^{2+}+Mg)$ ratios in olivine, and (X_{Fe}^{M1}) Opx and (X_{Fe}^{M2}) Opx refer to the atomic fractions of Fe in M1 and M2 sites of orthopyroxene (Wood, 1990).

The uncertainty in the calculated fO_2 originates from analytical errors and errors associated with activity estimates of components in Eq. (1). Analytical errors in silicate compositions contribute little to the fO_2 uncertainty. For example, olivine composition has an error of less than ±0.003 in X_{Fe}, which translates into an uncertainty of ±0.15 log units in fO_2. Orthopyroxene grains are more heterogeneous in composition than olivine in individual samples; however, propagated uncertainties from this heterogeneity are also small, on the order of 0.1 log units in fO_2 or less.

Inaccurate Fe^{3+} contents in spinel are the major cause of error in calculated fO_2 (O'Neill and Wall, 1987; Wood and Virgo, 1989). To alleviate this error, four secondary spinel standards with known Fe^{3+} contents were used to estimate $Fe^{3+}/\sum Fe$ of samples following the method by Wood and Virgo (1989). In this study, the calibrated $Fe^{3+}/\sum Fe$ ratios are systematically higher than those calculated assuming stoichiometric composition and charge balance (Fig. 3). We determined Fe^{3+} in the same way as Woodland et al. (1992), therefore we believe the uncertainty in $Fe^{3+}/\sum Fe$ is similar to their value, ±0.025. Combing the analytical error and error associated with using an activity model for Fe_3O_4 in spinel (see Eq. (2)), determination of spinel produces fO_2 uncertainty of 0.3–0.4 log units.

The calculation of fO_2 requires P and T, but estimates of P for spinel peridotites have large uncertainties because of no well-established

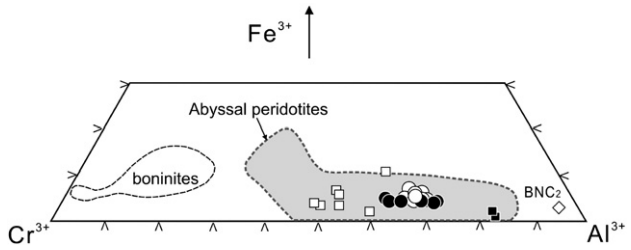

Fig. 5. Ternary diagram of Fe^{3+}–Cr^{3+}–Al^{3+} for spinel in the peridotite xenoliths from Pali Aike. Symbols are the same as in Fig. 4. Note that spinel grains in Pali Aike mantle xenoliths are generally low in Fe^{3+} and that their compositions overlap with the field of abyssal peridotites except for garnet orthopyroxenite. Field for abyssal peridotites is after Dick and Bullen (1984) and Barnes and Roeder (2001), and field for boninite is after Barnes and Roeder (2001).

Table 2
Bulk rock compositions of mantle xenoliths from Pali Aike area, southern Patagonia

Rock type	Grt-Spl lherzolite							Grt-Spl harzburgite							
Sample	LS33[a]	TM0	TM2	LS50	BN73	LS1	BN32	TM14	TM15	BN92	BN50	PAHK1	PAK6	BN45	BN31
Major (wt.%)															
SiO_2	44.69	44.24	44.20	43.87	43.04	44.02	45.00	44.01	44.49	46.74	42.76	44.38	45.18	45.58	45.62
TiO_2	0.12	0.14	0.16	0.16	0.05	0.10	0.18	0.17	0.13	0.29	0.18	0.15	0.32	0.18	0.20
Al_2O_3	3.14	4.18	3.73	1.97	1.53	2.57	3.86	3.47	3.12	3.80	3.84	3.62	3.16	3.89	3.64
Fe_2O_3 (t)[b]	8.78	9.17	9.02	9.30	9.10	8.95	9.21	10.35	10.73	9.70	10.59	10.52	11.98	9.93	10.11
MnO	0.13	0.14	0.14	0.12	0.12	0.13	0.13	0.14	0.14	0.13	0.14	0.14	0.14	0.14	0.13
MgO	40.41	38.35	39.25	41.02	44.54	41.13	38.19	40.75	40.52	38.40	40.65	40.20	38.57	39.13	39.60
CaO	2.43	3.33	2.86	2.83	1.24	2.29	2.97	1.09	0.99	1.04	1.21	0.68	0.66	0.87	0.75
K_2O	<0.02	<0.02	<0.02	<0.02	<0.02	<0.02	0.04	0.02	<0.02	<0.02	<0.02	<0.02	<0.02	<0.02	<0.02
Total	99.70	99.55	99.36	99.27	99.62	99.18	99.58	99.99	100.1	100.1	99.37	99.69	100.0	99.72	100.0
Mg# [c]	0.90	0.89	0.90	0.90	0.91	0.90	0.89	0.89	0.88	0.89	0.88	0.88	0.86	0.89	0.89
Minor (ppm)															
Cr	2800	2420	2780	2260	2360	2470	2620	2510	2540	2680	5440	2650	1730	2450	2170
Ni	1720	1740	1410	2370	2460	2250	1930	1700	1970	1550	1510	2190	2340	2330	2370

[a] Grt lherzolite.
[b] Total Fe reported as Fe2O3.
[c] Mg# = Mg/(Mg + total Fe).

geobarometer for garnet-free peridotites. For spinel peridotites we use 15 kb for the calculation. To mitigate the uncertainties of *PT* estimates, fO_2 is expressed relative to FMQ buffer. Errors of ±100 °C and ±8 kb produce uncertainties of only ±0.2 and ±0.3 log units in Δlog fO_2 (FMQ), respectively. Considering a normal distribution of error, overall uncertainties of Δlog fO_2 (FMQ) is about ±0.5 log units. For comparison, fO_2 values are also calculated using the formula of Ballhaus et al. (1991) (Table 4).

5. Mineral chemistry and bulk compositions of xenoliths

5.1. Mineral chemistry

5.1.1. Olivine

Olivine in garnet-spinel lherzolite has higher Fo (89–91) than that in garnet-spinel harzburgites (87–89) (Appendix 1), which is not consistent with the general interpretation that harzburgite is more refractory than lherzolite, and so low Fo values in harzburgites are attributed to metasomatism. Similar Fo values are observed in spinel lherzolite and spinel harzburgite, 90–91 and 86–92, respectively (Appendix 2). Relict olivine in orthopyroxenites shows low Fo, 83–87 (Appendix 3).

5.1.2. Orthopyroxene

As with olivine, the values of Mg# (=Mg/(Mg+ΣFe)) for orthopyroxene are higher (0.90–0.91) in lherzolite and lower (0.87–0.92) in harzburgites (Appendices 1 and 2). High Ti in orthopyroxene in harzburgites (0.13–0.35 wt.%) is another indication that harzburgites have been metasomatized. Orthopyroxenites contain orthopyroxene with low Mg# (0.85–0.89) and relatively high TiO_2 (0.20–0.59 wt.%) (Appendix 3). The Mg# of orthopyroxene is similar or slightly greater than that of olivine, confirming the equilibration between the two (Von Seckendorff and O'Neill, 1993).

5.1.3. Clinopyroxene

As in olivine and orthopyroxene, clinopyroxene in garnet-spinel harzburgites shows slightly lower Mg# (0.88–0.89), but significantly higher TiO_2 (0.90–1.26 wt.%) than that of garnet-spinel lherzolites (Mg# = 0.89–0.91; 0.11–0.64 wt.% TiO_2) (Appendix 1), again confirming that the harzburgites were metasomatized. Relict clinopyroxene occurs in secondary orthopyroxene in orthopyroxenites, but contains high TiO_2 (0.65–1.59 wt.%) and low Mg# (0.83–0.91) compared to that in peridotites (Appendix 3).

5.1.4. Oxides

Spinel, intergranular and inclusions in other minerals, has similar compositions in individual samples (Appendix 4), suggesting that spinel is equilibrated. Spinel in most peridotites plots in the field for abyssal peridotites on the binary Cr#-Mg# diagram and ternary Fe^{3+}–Cr^{3+}–Al^{3+} diagram (Figs. 4 and 5). Similar compositions for spinel in garnet-bearing lherzolites (0.27–0.37; Table 4) and harzburgites (0.29–0.33; Table 4) suggest that harzburgites are not typical mantle residues because refractory harzburgites should have higher Cr# in spinel (Dick and Bullen, 1984). Spinel in garnet-free peridotites shows variable compositions, low Cr# (~0.17) in lherzolites and high Cr# (0.36–0.50) in harzburgites (Table 4). Rare spinel in orthopyroxenite is characterized by low Cr (Table 4).

Ilmenite is common in orthopyroxenites, and in phlogopite veinlets in garnet-bearing peridotites. Ilmenite is characterized by high MgO (11.09–13.66 wt.%) (Appendix 3). The hematite components in ilmenite are low, 0.52–4.07 mol%, and no exsolution lamellae of hematite were observed.

5.1.5. Garnet

Garnet contains high Mg# (0.77–0.86) compared to that in orthopyroxenites (0.74–0.80) (Appendices 1 and 3). Garnet in garnet-spinel harzburgite and garnet orthopyroxenite contains significantly higher TiO_2 (0.18–0.42 wt.%) and lower Cr_2O_3 (0.39–1.63 wt.%) compared to those in lherzolite, which have TiO_2 and Cr_2O_3 at 0.05–0.25 wt.% and 1.21–1.93 wt.%, respectively (Appendices 1 and 3). There is no difference in composition between garnet grains with and without spinel inclusions.

5.1.6. Hydrous minerals

Orthopyroxenites and metasomatized harzburgites contain high Ti-phlogopite (up to 7.5 wt.% TiO_2) and amphibole (up to 4.8 wt.% TiO_2) (Appendix 3). Amphibole shows a large compositional variation in CaO (5.9–12.2 wt.%) and K_2O+Na_2O (1.77–8.93 wt.%), even within individual grains, which suggests their late formation without equilibration.

5.2. Bulk rock compositions of xenoliths

All lherzolites contain lower CaO and Al_2O_3 and higher Mg# (Mg/(Mg+ΣFe)) than the estimated primitive mantle composition (McDonough and Sun, 1995), confirming that they are residues of various degrees of partial melting (Table 2; Fig. 6). It was noted that most

Spl lherzolite		Spl harzburgite						Grt orthopyroxenite						
PA64	PAK1	LS5	PAK2	PAK3	LS100	PAK5	01BN	BNH13	BNC2	BNC1	BN43	BNO5	BNC3	BNH5
43.82	44.36	43.14	43.65	43.84	43.42	43.00	44.04	52.58	53.02	52.76	53.95	52.53	51.74	48.80
0.05	0.10	0.14	0.05	0.05	0.14	0.34	<0.05	0.46	0.84	1.20	0.70	0.55	2.00	0.29
1.64	2.09	1.22	0.98	0.95	1.15	1.51	1.40	5.65	4.28	4.05	3.62	5.22	4.57	11.34
9.53	8.40	10.21	8.03	8.13	10.32	13.52	8.88	9.07	10.56	9.53	8.64	9.69	9.74	9.66
0.14	0.12	0.12	0.11	0.11	0.12	0.13	0.13	0.14	0.13	0.11	0.12	0.13	0.12	0.19
43.52	41.69	43.95	45.59	46.05	44.08	40.92	44.47	30.24	29.93	30.71	31.93	30.34	30.68	26.80
1.23	2.56	0.31	0.94	0.67	0.41	0.46	0.85	1.54	0.92	0.93	0.91	1.04	0.78	2.19
<0.02	<0.02	<0.02	<0.02	<0.02	<0.02	<0.02	<0.02	0.27	0.14	<0.02	0.02	0.02	0.03	<0.02
99.9	99.3	99.1	99.4	99.8	99.6	99.9	99.8	100	99.8	99.3	99.9	99.5	99.7	99.3
0.90	0.91	0.90	0.92	0.92	0.89	0.86	0.91	0.87	0.85	0.86	0.88	0.86	0.86	0.85
1520	2230	2840	2760	2470	2770	2390	4080	2220	2060	2130	1840	2350	2740	2580
2190	2280	2500	2510	2590	2320	2720	2450	761	971	991	743	1110	1290	698

lherzolites and spinel harzburgites have similar major element compositions as abyssal peridotites (Fig. 6).

Most garnet-bearing harzburgites have higher SiO_2, Al_2O_3, TiO_2 and lower Mg# than that of spinel harzburgites (Fig. 6). Furthermore, they contain higher TiO_2 and lower Mg# than garnet-bearing lherzolites(Fig. 6a, c, d), suggesting that they were metasomatized. Three spinel harzburgite samples also show higher TiO_2 and lower Mg# than spinel lherzolites (Fig. 6c–d), suggesting that spinel harzburgites were also affected by similar metasomatism as in garnet-bearing harzburgites.

Garnet orthopyroxenites contain high SiO_2 (48.8–53.95 wt.%), Al_2O_3 (3.62–11.34 wt.%) and TiO_2 (up to 2.0 wt.%), and low Mg# (0.85–0.88) compared to peridotite xenoliths (Fig. 6).

5.3. Metasomatism

Metasomatic minerals are common in garnet-bearing samples (Table 1). Several garnet-bearing harzburgites contain veinlets of orthopyroxenite with halos of Ti minerals and secondary orthopyroxene (Fig. 2d). These veinlets have identical mineralogy and mineral chemistry as discrete garnet orthopyroxenite xenoliths, suggesting that these xenoliths were likely brought from wide veins of orthopyroxenites in the mantle. The orthopyroxenites are interpreted to be the products of extensive metasomatism of harzburgites based on the presence of relict olivine (Fig. 2e), mineral and bulk compositions. One orthopyroxenite contains relict clinopyroxene enclosed in orthopyroxene and is interpreted to have originated from lherzolite (Fig. 2f). Although it is difficult to evaluate the abundance of orthopyroxenite in the mantle, it is probably minor in the mantle considering that both veined xenoliths and orthopyroxenites comprise <10% of all xenoliths. Olivine has low Fo and plots outside or on the margin of the olivine-spinel mantle array of Arai (1994) (Fig. 7).

Cryptic metasomatism is expressed as low Mg# and elevated TiO_2 in minerals and bulk rock compositions (Figs. 6c–d and 8). Lower Mg# and higher TiO_2 in olivine and pyroxenes in harzburgites than those in lherzolites suggest prevalent metasomatism in harzburgites (Fig. 8).

Metasomatism in spinel peridotites is not as common as in garnet-bearing peridotites. Only one spinel lherzolite sample (PA64) contains a websterite veinlet, and two spinel harzburgites (PAK5, LS100) show high

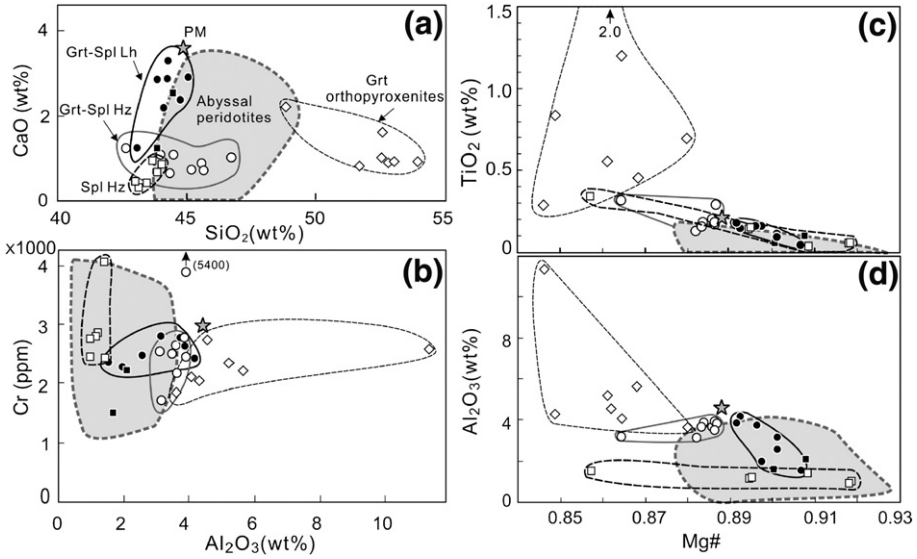

Fig. 6. Bulk chemical compositions of mantle xenoliths from the Pali Aike area. Plots of (a) CaO vs. SiO_2, (b) Cr vs. Al_2O_3, (c) TiO_2 vs. Mg# and (d) Al_2O_3 vs. Mg# for bulk compositions of mantle xenoliths from Pali Aike. Filled star depicted with PM refers to the primitive mantle composition (McDonough and Sun, 1995). Fields for abyssal peridotites are based on the data of Niu (2004). Other symbols are the same as in Fig. 4. Note that garnet orthopyroxenites show a wide compositional variation; spinel harzburgite shows a wide compositional variation in subpanels (c) and (d).

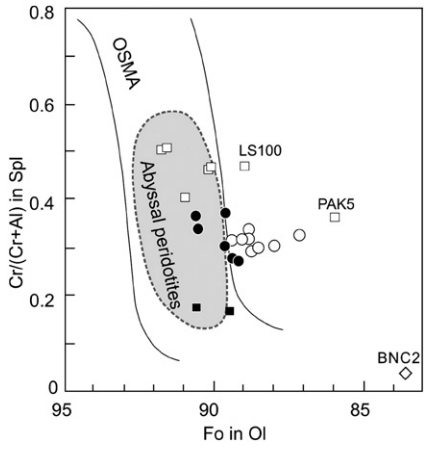

Fig. 7. Fo component of olivine and Cr# of spinel in peridotite xenoliths from Pali Aike. Symbols are the same as Fig. 4. Note that all garnet-spinel harzburgites, two spinel harzburgites and one orthopyroxenite (BNC2) plot outside the olivine-spinel mantle array (OSMA) defined by Arai (1994), suggesting that they are not primary mantle peridotites. It also shows the field of abyssal peridotite as a shaded area (Arai, 1994).

TiO_2 and low Mg# in bulk and mineral compositions (Figs. 6 and 8). The nature of metasomatism is similar to that in garnet-bearing peridotites, suggesting a similar metasomatizing agent for garnet and spinel peridotites.

Considering the formation of Ti-rich minerals and high TiO_2 and low Mg# in bulk rocks, we suggest that the metasomatizing melt is an evolved melt that originated from the asthenospheric mantle. The metasomatizing agent is cogenetic with the host Pali Aike alkali basalts, but the host basaltic magmas cannot be the metasomatizing agent because the host magmas are primitive with high Mg#. Therefore they cannot lower Mg# of the peridotites. The cogenetic nature of the metasomatizing melt is supported by Sr and Nd isotopic compositions for metasomatized garnet-spinel harzburgites that are similar to those of Pali Aike host basalts and other Patagonian plateau alkali basalts (Kempton et al., 1999b; Stern et al., 1999).

6. Pressure, temperature and fO_2

Mg# of coexisting minerals show positive correlations in individual samples except for two garnet-bearing harzburgites (TM14, TM15). The data suggest that most minerals were equilibrated. This is a valid basis for estimating equilibrium *PT* conditions and fO_2 of these xenoliths. Temperatures for peridotite xenoliths were determined using two-pyroxene thermometers (Wells 1977; Brey and Köhler, 1990) and Ca-in-Opx thermometry (Brey and Köhler, 1990) (Table 3). The two-pyroxene thermometry of Brey and Köhler (1990) yielded systematically higher *T* by up to ~100 °C than the results using the Wells' thermometry. The Ca-in-Opx thermometry (Brey and Köhler, 1990) gave similar *T*, only slightly higher *T* by approximately 5 °C, as the two-pyroxene thermometry of Wells (1977). The olivine-spinel Fe–Mg exchange thermometry of Ballhaus et al. (1991) gave systematically lower *T* than other thermometers, most likely due to lower closure *T* for ion exchange between spinel and olivine (e.g., DeHoog et al., 2004). Wells' thermometry was used for fO_2 calculations in this study because it has been used for fO_2 calculations of mantle peridotites by previous workers (e.g., Wood and Virgo, 1989; Ionov and Wood, 1992). For those samples without clinopyroxene, the *T* using the Ca-in-Opx thermometry was used after subtracting the systematic difference of 5 °C between the two thermometers.

Al-in-Opx barometry by Mercier (1980) for garnet-free samples yielded *P* ranging from 11.6 to 22.6 kb with a median value at 15 kb (Table 3). For garnet peridotites, Al-in-Opx barometry by Nickel and Green (1985) yielded systematically lower *P* by 2–7 kb than that by Brey and Köhler (1990) (Table 3). This paper uses the *P* based on the barometry of Nickel and Green (1985). The estimated *P* and *T* (Table 3) for the Pali Aike xenoliths are generally consistent with previous results (Kempton et al., 1999a; Stern et al., 1999). Garnet-free samples show low *P* and similar *T* when compared with garnet-bearing samples and did not yield a continuous geotherm. The geotherm based on garnet-bearing peridotites is much higher than those of ancient cratons, such as South Africa, Siberia and Namibia (Fig. 9), but similar to oceanic geotherm and those of off-craton areas affected by upwelling asthenospheric mantle, such as Vitim, Russia (Ionov et al., 1993) and SE China (Qi et al., 1995) (Fig. 9). Stern et al. (1999) suggested that this high geotherm was a relic inherited from the late Jurassic rifting related to the break-up of Gondwana and the opening of the southern Atlantic ocean. On the other hand, Kempton et al. (1999b) suggested that high geotherm in the region is linked to a late Tertiary–Neogene event. We suggest that the observed high geotherm defined by garnet-bearing peridotites is most likely related to hot asthenospheric upwelling through a slab window in the area since Tertiary.

The calculated fO_2 values of peridotites range from FMQ−0.33 to FMQ+0.75 and the majority of samples are slightly more oxidized than the FMQ buffer, with the median value of FMQ +0.30 (n=24) (Table 4). Garnet-bearing lherzolite and harzburgite show similar mean fO_2 values of FMQ+0.13±0.32 (n=6) and FMQ+0.22±0.19 (n=8), respectively. Orthopyroxenite sample BNC2 shows relatively reduced fO_2 value of FMQ−0.50.

7. Discussion

7.1. Origin and evolution of the mantle below southern Patagonia

7.1.1. Formation of SCLM below Pali Aike

Several possible processes have been proposed for the formation of SCLM, including formation of highly refractory lithospheric mantle above mantle plumes (Herzberg, 1999), formation of highly refractory mantle in mantle wedges (Parman et al., 2004), and accretion of oceanic lithosphere (Boyd, 1989; Niu and O'Hara, 2003). The oceanic

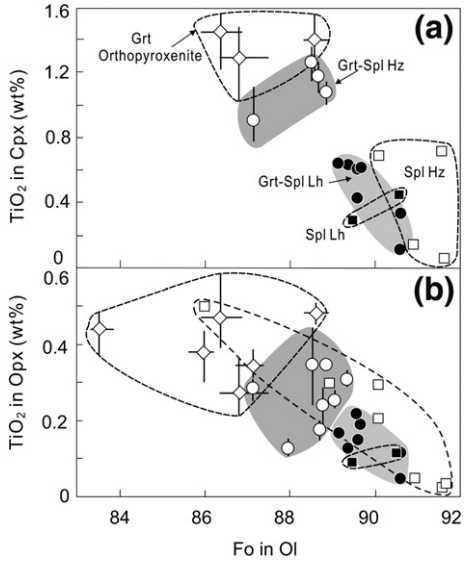

Fig. 8. Plots of TiO_2 in pyroxenes and Fo in olivine in mantle xenoliths from the Pali Aike area. Symbols for samples are the same as in Fig. 4. Note that orthopyroxenites, garnet-spinel harzburgites and several spinel harzburgites show low Fo in olivine and high TiO_2 contents in clinopyroxene and orthopyroxene compared with their lherzolites counterparts. The variation bars shown in orthopyroxenites and garnet-spinel harzburgites are based on 3–5 analyses.

lithosphere accretion model involves the thickening of lithosphere mantle by stacking oceanic lithosphere during subduction (Boyd, 1989; Niu and O'Hara, 2003). The mantle plume model involves upwelling of hot asthenospheric mantle plume followed by high degree of partial melting above plume heads to form buoyant refractory lithospheric mantle. The mantle wedge model suggests that continents and underlying lithospheric mantle may be formed from refractory wedge mantle (Parman et al., 2004). This model explains the occurrence of subduction-related igneous rocks in ancient continents (Canil, 2004), the Si-enrichment in SCLM (Kelemen et al., 1998), and small volumes of volcanic rocks to mass balance the refractory composition of SCLM. The model also explains the enrichment of incompatible trace elements in continental rocks (Carlson et al., 2005).

Both "hot plume" and "mantle wedge" models require partial melting to form refractory SCLM and the age of SCLM should be older than or similar to voluminous igneous rocks on the overlying continent. However, Pali Aike peridotites are not as refractory as most ancient SCLM. Peridotites from ancient SCLM, such as Kaapvaal and Siberian cratons, commonly show high Fo of olivine with an average of 93 (Boyd, 1989; Boyd et al., 1997) and high Cr#, 0.49–0.79, in spinel (Woodland and Koch, 2003). The data suggest that these two models may not be applicable to the formation of the SCLM underlying Pali Aike.

The degrees of partial melting and origin of peridotites can be evaluated by examining the ratios of Mg/Si and Al/Si of bulk rock compositions (e.g., Hattori and Guillot, 2007). Un-metasomatized Pali Aike peridotites show lower Mg/Si and higher Al/Si than refractory sub-arc peridotites and plot in the field of abyssal peridotites (Fig. 10). The degree of depletion due to melt extraction in the residual mantle can also be illustrated in a diagram of Al_2O_3 in orthopyroxene vs Cr# in spinel (Fig. 11). Preferential incorporation of Al in melt lowers Al^{VI} in orthopyroxene and increases Cr# in spinel in the residues. Un-metasomatized garnet-bearing lherzolites and most spinel peridotites in Pali Aike show Al_2O_3 contents in Opx and Cr# in spinel overall overlapping with the field of abyssal peridotites, and notably higher Al in Opx and lower Cr in spinel than sub-arc peridotites, such as Mariana (Bloomer and Hawkins, 1983; Parkinson and Pearce, 1998), Tonga (Bloomer and Fisher, 1987), and south Kamchatka (Arai et al., 2003). In addition, compositions of spinel in anhydrous peridotite xenoliths plot in the field of abyssal peridotites in both the binary (Mg#–Cr#) and ternary (Fe^{3+}–Cr^{3+}–Al^{3+}) diagrams (Figs. 4 and 5).

Therefore our data support the suggestion that the SCLM beneath the Pali Aike formed from an oceanic lithosphere. This interpretation is also supported by similar abundance and normalized patterns of REE and Sr–Nd isotope compositions between garnet lherzolites and abyssal peridotites (Stern et al., 1999; Kempton et al., 1999b). Considering the Re–Os model ages of 531 Ma (sample TM2) and 860 Ma (sample LS33) for Pali Aike garnet peridotites (Stern et al., 1999), the SCLM beneath Pali Aike may have formed from oceanic lithosphere that was produced at a ridge in late Proterozoic–early Paleozoic time (Fig. 12).

The Pali Aike area occurs south of the Deseado Massif of southern Patagonia. There are arc igneous rocks of Siluro-Devonian time along

Table 3
Temperature and pressure estimates for the peridotite xenoliths from Pali Aike area, southern Patagonia

Sample	Rock type	Temperature (°C)				*P* (kb)		
		Wells (1977)[a]	B&K (1990)[b]	B&K(1990)[c]	Ballhaus et al. (1991)[d]	B&K (1990)[e]	N&G (1985)[f]	Mercier (1980)[g]
LS33	Grt-Spl lherzolite	1110	1209	1121		27.0	23.2	
TM0		959	1011	984	922	21.8	19.6	
TM2		964	1040	965	915	23.4	20.8	
LS50		1015	1099	1035	945	25.5	22.0	
BN73		1055	1133	1073	1020	27.3	22.1	
LS1		1074	1127	1043	940	29.1	22.7	
BN32		1001	1051	993	875	23.8	20.1	
TM14	Grt-Spl harzburgite	959	1027	993	917	22.8	21.1	
TM15				965	902	21.1	19.3	
BN92		1006	1073	1010	986	23.5	21.4	
BN50		980	1061	1019	951	23.6	20.9	
PAHK1				1010	938	23.0	20.8	
PAK6		1125	1165	984	895	30.3	24.9	
BN45				1035	900	25.2	20.8	
BN31				993	933	23.6	21.4	
PA-64	Spl lherzolite	777	685	891	801			12.7
PAK1		849	836	951	784			12.9
LS5	Spl harzburgite			994	977			14.9
PAK2		997	1030	1018	959			15.5
PAK3		1024	1066	1010	952			15.0
LS100				108	975			17.8
PAK5				1025	1057			16.8
01BN		909	882	880	672			11.6
BNH11		1055	1103	986	831			22.6
BNO5	Grt orthopyroxenite			1024		22.8	20.9	
BN92		988	1077	1014		22.5	20.6	
BNH13		1069	1150	1005		26.5	24.6	
BN46		984	1079	1033		22.9	21.6	
BNH5		1064	1170	984		26.1	24.8	
BN43	Grt-absent orthopyroxenite			932				20.11
BNC1		1043	1131	1002				22.54
BNC2				1002				22.48

[a] Wells (1977) two-pyroxene thermometer.
[b] Brey and Köhler (1990) two-pyroxene thermometer.
[c] Brey and Köhler (1990) Ca-in-Opx thermometer.
[d] Ballhaus et al. (1991) Ol-Spl Mg–Fe exchange thermometer.
[e] Brey and Köhler (1990) Al-in-Opx barometer.
[f] Nickel and Green (1985) Al-in-Opx barometer.
[g] Mercier (1980) Al-in-Opx barometer.

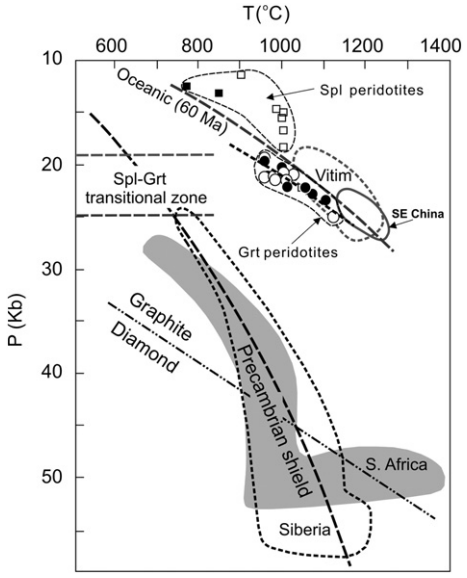

Fig. 9. Results of thermobarometries of peridotite xenoliths in this study. Symbols are the same as in Fig. 4. Our data of garnet-bearing samples define a continuous geotherm, close to the oceanic geotherm for 60 Ma old plate. Oceanic geotherm, Precambrian shield geotherm, and fields for Archean SCLM at S. Africa, Siberia and Namibia are from Nickel and Green (1985). Data for Phanerozoic SCLM at Vitim, Russia is from Ionov et al. (1993). Data for Phanerozoic SCLM at SE China is from Qi et al. (1995). The location of graphite-diamond phase transition is from Kennedy and Kennedy (1976). The spinel-garnet transitional zone is based on this study.

the southeastern margin of the Deseado massif (Pankhurst et al., 2006), suggesting the development of a subduction complex in response to the northern subduction of oceanic lithosphere along the southern margin of the Deseado Massif (Fig. 12a). Like many oceanic subduction zones, this oceanic subduction zone was likely accompanied by an accretionary prism of sediments and a stack of underplated oceanic lithosphere (Fig. 12b), which we suggest became the SCLM below Pali Aike. The proposed scenario is consistent with Re–Os model ages of late Proterozoic and early Paleozoic age of mantle xenolith samples (Stern et al., 1999; Schilling et al., 2008).

Subduction of the Nazca plate resulted in the formation of a continental arc along the west coast of southernmost South America in Miocene time (Fig. 12c). This was followed by the collision of Chile ridge with the trench at ~14–15 Ma (Cande and Leslie, 1986; Fig. 12d). The ridge subduction resulted in the formation of a slab window and the extensive eruption of plateau lavas from late Miocene to Recent (e.g., Gorring et al., 1997; D'Orazio et al., 2000). Asthenospheric mantle-derived melt infiltrated the lower portions of overlying SCLM and metasomatized garnet-bearing peridotites (Fig. 12d).

7.1.2. Origin of garnet-bearing peridotites

Two possible processes are proposed to explain the common occurrence of relict spinel in garnet (Fig. 2c); cooling or *P* increase. Either cooling or *P* increase results in the isochemical reaction of spinel + orthopyroxene + clinopyroxene forming garnet + olivine (Obata and Morten, 1987). Stern et al. (1999) suggested cooling greater than 175 °C based on core-to-rim compositional zoning in clinopyroxene from Pali Aike spinel lherzolites, and suggested that this cooling caused spinel break-down to form garnet and olivine either in the late Proterozoic or early Paleozoic, or after the late Jurassic opening of the southern Atlantic ocean. Granulite xenoliths in the Pali Aike basalts considered to have formed during the Jurassic event associated with the opening of the southern Atlantic ocean underwent similar post-crystallization cooling (Selverstone and Stern, 1983). Most likely explanation for the occurrence of relic spinel in garnet is a pressure increase during subduction/accretion of oceanic lithosphere. The subduction and accretion of oceanic lithosphere results in pressure increase which led to the transformation from spinel- to garnet-facies peridotites (Fig. 12b).

7.2. Possible processes controlling the oxidation states of mantle rocks

The variable lithologies, a range in Cr# in spinel and the evidence of metasomatism in our samples suggest that the redox state may have been influenced by both partial melting in the original suboceanic lithosphere and the subsequent metasomatism associated with the generation of the Pali Aike basalts. Partial melting is considered to result in reduction of fO_2 in the residual mantle as Fe^{3+} is preferentially incorporated in partial melt (Canil et al., 1994). However, our spinel-facies xenolith samples, which are in general free of metasomatism, do not show any correlation between fO_2 and Cr# of spinel (Fig. 13), suggesting that their fO_2 did not change during partial melting. Our results are consistent with comparable fO_2 values between mid-oceanic ridge basalts and the abyssal peridotites (Christie et al., 1986; Bézos and Humler, 2005). This conclusion is also supported by the experimental result of Amundsen and Neumann (1992), who showed that garnet-facies mantle peridotites produce a partial melt with comparable $Fe^{3+}/\Sigma Fe$ ratios.

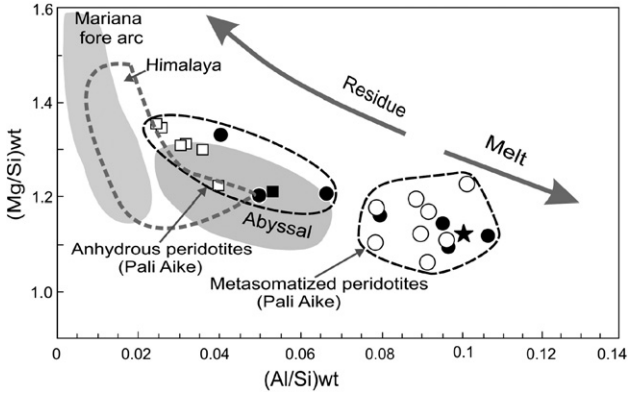

Fig. 10. Weight ratio of Mg/Si vs. Al/Si of peridotites in Pali Aike area. The large solid star represents primitive mantle value from McDonough and Sun (1995). The fields for abyssal peridotites, Himalaya peridotites, and Mariana forearc peridotites are from Hattori and Guillot (2007). The compositional variation expected during partial melting is shown with arrows. Residues have higher Mg/Si and lower Al/Si, whereas melt has a lower Mg/Si and higher Al/Si. Symbols are the same as in Fig. 4. Note that un-metasomatized peridotites overall overlap with the field of abyssal peridotites.

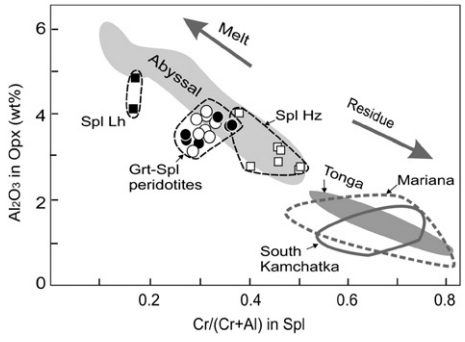

Fig. 11. Plot of Al_2O_3 in Opx (wt.%) vs. Cr# in spinel for peridotites in Pali Aike area. The field for abyssal peridotites is based on the samples from North Atlantic oceanic peridotites by Michael and Bonatti (1985). Data source for arc mantle peridotites includes Mariana (Bloomer and Hawkins, 1983; Parkinson and Pearce, 1998), Tonga (Bloomer and Fisher, 1987), and south Kamchatka (Arai et al., 2003). The mineral compositional variation expected during partial melting is shown with arrows. Residues have higher Cr# in spinel and lower Al_2O_3 in Opx. Symbols are the same as in Fig. 4. Note the spinel peridotites and un-metasomatized garnet-spinel peridotites in Pali Aike overall overlap with the field of abyssal peridotites, and show notable high Al in Opx and low Cr in spinel compared with mantle wedge peridotites.

Table 4
Estimates of oxygen fugacity values for the mantle xenoliths from Pali Aike, southern Patagonia

Lithology	Grt-Spl lherzolite						Grt-Spl harzburgite								Spl lherzolite		Spl harzburgite							Grt orthopyroxenite
sample	TM0	TM2	LS50	BN73	LS1	BN32	TM14	TM15	BN92	BN50	PAHK	PAK6	BN45	BN31	PA64	PAK1	LS5	PAK2	PAK3	LS100	PAK5	01BN	BNH11	BNC2
Olivine																								
X_{Fe}	0.11	0.10	0.10	0.09	0.09	0.11	0.11	0.12	0.11	0.11	0.11	0.13	0.11	0.11	0.11	0.09	0.10	0.08	0.08	0.11	0.14	0.09	0.10	0.16
X_{Mg}	0.89	0.90	0.90	0.91	0.91	0.89	0.89	0.88	0.89	0.89	0.89	0.87	0.89	0.89	0.89	0.91	0.90	0.92	0.92	0.89	0.86	0.91	0.90	0.84
Orthopyroxene																								
$M1_{(Fe)}$[a]	0.09	0.09	0.09	0.08	0.06	0.07	0.09	0.10	0.10	0.09	0.09	0.11	0.07	0.09	0.09	0.08	0.07	0.07	0.07	0.10	0.12	0.08	0.07	0.14
$M2_{(Fe)}$[a]	0.10	0.10	0.10	0.09	0.07	0.08	0.09	0.10	0.10	0.09	0.10	0.12	0.08	0.10	0.10	0.09	0.07	0.07	0.08	0.10	0.13	0.09	0.08	0.15
Spinel																								
Cr#	0.28	0.30	0.37	0.34	0.36	0.27	0.29	0.30	0.29	0.33	0.31	0.32	0.31	0.31	0.17	0.17	0.46	0.50	0.50	0.47	0.36	0.40	0.46	0.05
$Fe^{3+}/\Sigma Fe$[b]	0.29	0.29	0.30	0.34	0.31	0.29	0.29	0.28	0.34	0.31	0.34	0.33	0.32	0.31	0.24	0.17	0.31	0.27	0.27	0.32	0.39	0.17	0.22	0.24
$Mg/(Mg+Fe^{2+})$	0.75	0.74	0.72	0.77	0.74	0.73	0.72	0.70	0.72	0.71	0.71	0.65	0.71	0.71	0.76	0.78	0.69	0.73	0.73	0.65	0.64	0.63	0.64	0.76
$\log a_{Fe_3O4}^{Spl}$	−1.74	−1.77	−1.76	−1.86	−1.87	−1.70	−1.67	−1.65	−1.59	−1.65	−1.58	−1.55	−1.63	−1.65	−1.56	−2.09	−1.66	−2.02	−2.04	−1.62	−1.32	−2.02	−1.99	−1.65
P (kbar)[c]	19.6	20.8	22.0	22.1	22.7	20.1	21.1	19.3	21.4	20.9	20.8	24.9	20.8	21.4	15.0	15.0	15.0	15.0	15.0	15.0	15.0	15.0	15.0	21.3
T °C(Wells)[d]	959	964	1015	1060	1074	1000	959	960	1010	980	1010	1130	1030	988	777	849	946	997	1020	1010	1020	909	1060	994
T (°C)[e]	922	915	945	1020	940	875	917	902	986	951	938	895	900	933	801	784	977	959	952	975	1057	672	831	1000
$\Delta\log(fO_2)FMQ$[f]	0.11	0.10	0.22	0.15	0.21	0.28	0.19	0.20	0.56	0.35	0.56	0.52	0.61	0.33	0.05	−0.59	0.77	0.15	0.17	0.81	1.19	0.01	0.36	−0.58
$\Delta\log(fO_2)FMQ$[g]	0.27	0.32	0.35	0.39	−0.23	−0.33	0.05	0.03	0.41	0.13	0.47	0.44	0.04	0.17	0.59	−0.13	0.11	0.41	0.48	0.66	0.75	0.32	−0.23	−0.50

[a] $M1_{(Fe)}$, $M2_{(Fe)}$ = fractions of Fe at M1 and M2 sites, calculated following the method in Wood (1990).
[b] Calibrated using the four spinel grains with known Fe^{3+} contents.
[c] For garnet-bearing xenoliths, P is calculated based on Al-in-Opx barometer of Nickel and Green (1985) and for garnet-free xenoliths P is assumed as 1.5 Gpa in fO_2 calculation.
[d] For xenoliths containing both Opx and Cpx, T is calculated based on two-pyroxene thermometer (Wells, 1977), and for samples without Cpx, T is calculated based on Ca-in-Opx thermometery (Brey and Köhler, 1990).
[e] Calculated based on Ol-Spl Fe–Mg exchange thermometer of Ballhaus et al. (1991).
[f] fO_2 estimates following the method of Ballhaus et al. (1991) using Fe^{3+} contents of spinel calculated from its stoichiometric composition.
[g] fO_2 estimates following the method of Nell and Wood (1991) using the calibrated contents of Fe^{3+}.

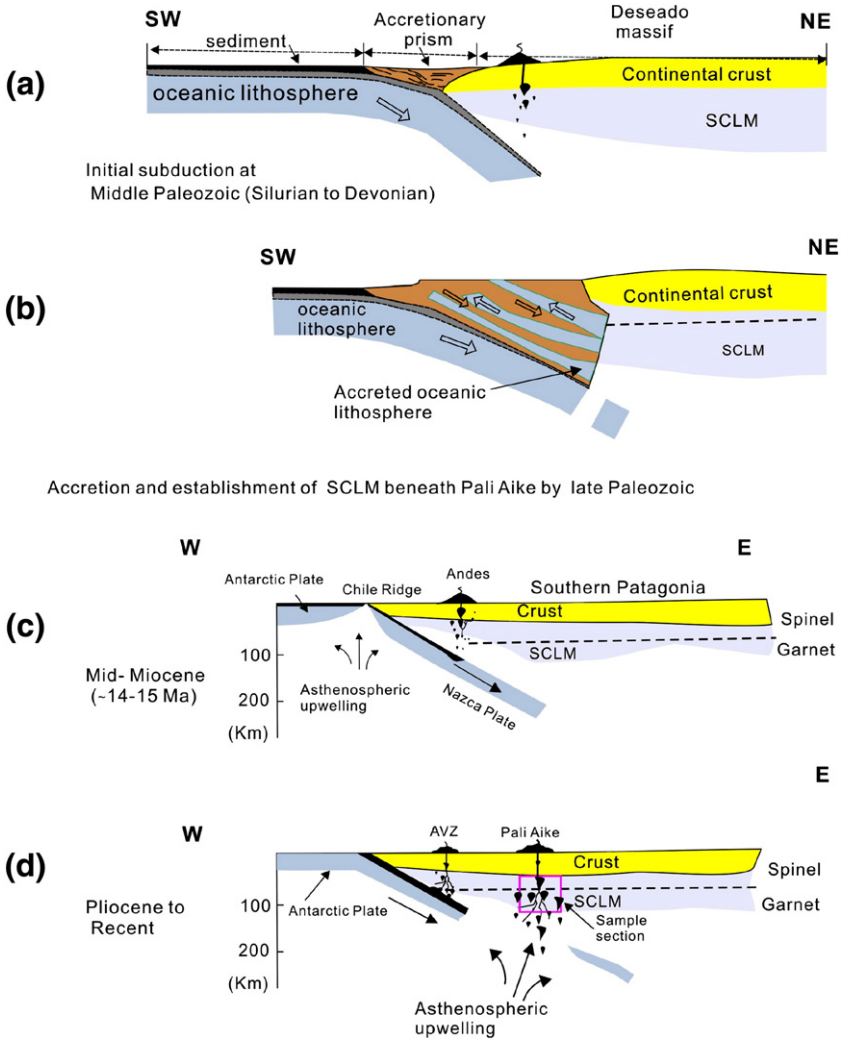

Fig. 12. Schematic diagrams showing the formation and later modifications of SCLM beneath Pali Aike, southern Patagonia. (a) An oceanic plate was subducted beneath the southeastern margin of Deseado Massif, South Patagonia during the Mid Paleozoic producing arc-type igneous rocks. The subduction resulted in the formation of accretionary prism. (b) Oceanic lithosphere was accreted to the southeastern margin of Deseado Massif by underthrusting and the SCLM beneath Pali Aike was established by late Paleozoic. (c) Eastward subduction Chile ridge collided with the trench at middle Miocene, ~14–15 Ma. (d) Chile ridge subducted beneath the Pali Aike volcanic field forming a slab window from which asthenospheric melt infiltrated the lower portions of overlying SCLM and erupted to the surface as Pali Aike volcanic rocks.

Orthopyroxenites represent the products of extensive metasomatism by melts. Therefore, fO_2 value of orthopyroxenites likely reflects the oxidation state of these metasomatizing melts. One orthopyroxenite (BNC2) yielded fO_2 of FMQ−0.50 based on spinel+orthopyroxene +olivine oxybarometry. Low contents of Fe^{3+} in ilmenite and clinopyroxene also support relatively reduced fO_2 for the metasomatizing agent for the formation of orthopyroxenites. Hematite components

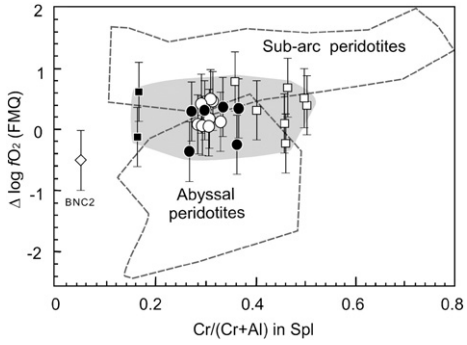

Fig. 13. Values of fO_2 relative to FMQ buffer (ΔfO_2 (FMQ)) vs. Cr# in spinel for peridotites from Pali Aike compared with abyssal peridotites (Bryndzia and Wood, 1990) and sub-arc mantle peridotites. Symbols are the same as Fig. 4. Sub-arc mantle peridotites include those from Ichinomegata in Japan, Marelava in Vanuatu arc, Grenada in Lesser Antilles arc, Santa Isabel and San Jorge in Solomon islands and the Simcoe area in Cascade arc (Wood and Virgo, 1989; Ballhaus et al., 1991; Brandon and Draper, 1996; Parkinson and Arculus, 1999; Parkinson et al., 2003).

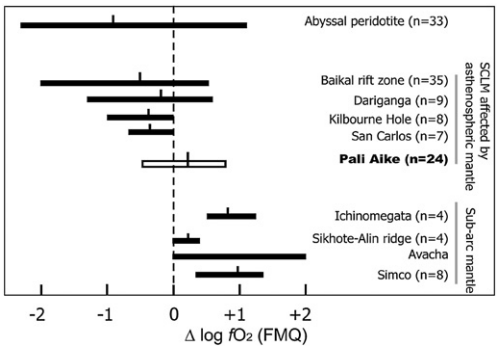

Fig. 14. Oxidation state for mantle xenoliths from Pali Aike in comparison with those for other mantle peridotites. Data source: abyssal peridotite (Bryndzia and Wood, 1990); Baikal rift zone, Dariganga, and Sikhote-Alin ridge (Ionov and Wood, 1992); Kilbourne Hole, San Carlos and Ichinomegata (Wood and Virgo, 1989); Avacha (Arai et al., 2003); Simcoe (Parkinson and Arculus, 1999). The vertical bar indicates the mean $\Delta \log fO_2$ (FMQ) value for a particular region.

in ilmenite range from 0.01 to 0.024, suggesting a relatively reduced fO_2 below FMQ (Frost et al., 1988). Clinopyroxene contains low $Fe^{3+}/\Sigma Fe$ below 0.067. An experimental study shows low Fe^{3+} contents in clinopyroxene that crystallizes under fO_2 below the FMQ buffer (McCanta et al., 2004). Furthermore, the oxidation state, lower than FMQ−0.3, is reported by D'Orazio et al. (2000) for the parental magmas of Pali Aike basalts. Low fO_2 value of the metasomatizing melt is consistent with relatively low fO_2 of the upper asthenospheric mantle, which is slightly reduced compared to the FMQ buffer as indicated by the data from abyssal peridotites (Bryndzia and Wood, 1990) and mantle peridotites in continental rifts that have been affected by asthenosphere-derived melts (Ionov and Wood, 1992).

The values of fO_2 for spinel-facies and garnet-facies peridotites are similar ranging from FMQ−0.33 to +0.75, suggesting that the transformation from spinel- to garnet-facies was not accompanied by fO_2 changes. The ranges of fO_2 for metasomatized (FMQ−0.33 to +0.75), un-metasomatized (FMQ−0.23 to +0.75) samples are also similar, suggesting that the later infiltration of asthenospheric melt did not alter fO_2 (Table 4; Fig. 13).

8. Conclusions

Pali Aike xenoliths show fO_2 values, FMQ−0.33 to +0.75, slightly elevated, but comparable to abyssal peridotites and other SCLM affected by asthenospheric mantle melt, such as Baikal rift zone in Russia (Ionov and Wood, 1992), Dariganga in Mongalia (Ionov and Wood, 1992), Kilbourne Hole and San Carlos in USA (Wood and Virgo, 1989), and western Victoria in Australia (Chen et al., 1991) (Figs. 13 and 14). The values are distinctly higher than fO_2 values of ancient SCLM underlying cratons. The fO_2 data together with bulk rock compositions of not-metasomatized samples support the formation of SCLM underlying the southern Patagonia through the accretion of oceanic lithosphere. Relict spinel in garnet-bearing peridotites suggests spinel-facies transformed to garnet-facies peridotites during the accretion. The formation of a slab window since late Tertiary resulted in the upwelling of asthenospheric-derived melt and extensive metasomatism of the peridotites, especially garnet-bearing facies. The metasomatized melt is characterized by high Al_2O_3, SiO_2, TiO_2 and FeO, and relatively reduced fO_2, ~FMQ−0.50. This metasomatizing melt did not significantly change the oxidation state of Pali Aike peridotites because their fO_2 values are comparable to that of the metasomatizing melt.

Acknowledgements

This work was supported by a Natural Science and Engineering Research Council of Canada (NSERC) Discovery grant to KHH and an Ontario Graduate Scholarship in Science and Technology and a PhD Admission Scholarship of the University of Ottawa to JW. We thank P. Jones at Carleton University and L. Shi at McGill University for their help during the electron microprobe analyses and B.J. Wood for allowing us to use his reference spinel grains. Thanks are also given to R. Hartree for his XRF analysis and George Mrazek for making thin sections at the University of Ottawa. The manuscript benefited from the constructive comments by A.C. Kerr, M. D'Orazio and an anonymous journal reviewer.

Appendix A. Supplementary data

Supplementary data associated with this article can be found, in the online version, at doi:10.1016/j.lithos.2008.02.009.

References

Amundsen, H.E.F., Neumann, E.-R., 1992. Redox control during mantle/melt interaction. Geochimica et Cosmochimica Acta 56, 2405–2416.
Arai, S., 1994. Characterization of spinel peridotites by olivine-spinel compositional relationships: review and interpretation. Chemical Geology 111, 191–204.
Arai, S., Ishimaru, S., Okrugin, V.M., 2003. Metasomatized harzburgite xenoliths from Avacha volcano as fragments of mantle wedge of the Kamchatka arc: implication for the metasomatic agent. The Island Arc 12, 233–246.
Ballhaus, C., 1993. Redox states of lithospheric and asthenospheric upper mantle. Contributions to Mineralogy and Petrology 114, 331–348.
Ballhaus, C., Berry, R.F., Green, D.H., 1991. High pressure experimental calibration of the olivine-orthopyroxene-spinel oxygen geobarometer: implications for the oxidation state of the upper mantle. Contributions to Mineralogy and Petrology 107, 27–40.
Barnes, S.J., Roeder, P.L., 2001. The range of spinel compositions in terrestrial mafic and ultramafic rocks. Journal of Petrology 42, 2279–2302.
Bézos, A., Humler, E., 2005. The Fe^{3+}/SFe ratios of MORB glasses and their implications for mantle melting. Geochimica et Cosmochimica Acta 69, 711–725.
Bloomer, S.H., Hawkins, J.W., 1983. Gabbroic and ultramafic rocks from Mariana Trench: an island arc ophiolite. Tectonic and Geological Evolution of the SE Asian Seas and Islands. American Geophysical Union Geophysical Monograph, vol. 27, pp. 234–316.
Bloomer, S.H., Fisher, R.J., 1987. Petrology and geochemistry of igneous rocks from the Tonga Trench, a non-accreting plate boundary. Journal of Geology 95, 469–495.
Boyd, F.R., 1989. Compositional distinction between oceanic and cratonic lithosphere. Earth and Planetary Science Letters 96, 15–26.
Boyd, F.R., Pokhilenko, N.P., Pearson, D.G., Mertzman, S.A., Sobolev, N.V., Finger, L.W., 1997. Composition of the Siberian cratonic mantle: evidence from Udachnaya peridotite xenoliths. Contributions to Mineralogy and Petrology 128, 228–248.
Brandon, A.D., Draper, D.S., 1996. Constraints on the origin of the oxidation state of mantle overlying subduction zones: an example from Simcoe, Washington, USA. Geochimica et Cosmochimica Acta 60, 1739–1749.
Brey, G.P., Köhler, T., 1990. Geothermobarometry in four-phase lherzolites: II. New thermobarometers, and practical assessment of existing thermobarometers. Journal of Petrology 31, 1353–1378.
Bruhn, R.L., Stern, C.R., de Wit, M.J., 1978. Field and geochemical data bearing on the development of a Mesozoic volcanic-tectonic rift zone and back arc basin in southernmost South America. Earth and Planetary Science Letters 41, 32–46.
Bryndzia, L.T., Wood, B.J., 1990. Oxygen thermobarometry of abyssal spinel peridotites: the redox state and C–H–O volatile composition of the Earth's sub-oceainc upper mantle. The American Journal of Science 290, 1093–1116.
Cande, S.C., Leslie, R.B., 1986. Late Cenozoic tectonics of the Southern Chile Trench. Journal of Geophysical Research 91, 471–496.
Canil, D., 1997. Vanadium partitioning and the oxidation state of Archean komatiite magmas. Nature 389, 842–845.
Canil, D., 2002. Vanadium in peridotites, mantle redox and textonic environments: Archean to present. Earth and Planetary Science Letters 195, 75–90.
Canil, D., 2004. Mildly incompatible elements in peridotites and the origins of mantle lithosphere. Lithos 77, 375–393.
Canil, D., O'Neill, H.St.C., Pearson, D.G., Rudnick, R.L., McDonough, W.F., Carswell, D.A., 1994. Ferric iron in peridotites and mantle oxidation states. Earth and Planetary Science Letters 13, 205–220.
Carlson, R.W., Pearson, D.G., James, D.E., 2005. Physical, chemical, and chronological characteristics of continental mantle. Reviews of Geophysics 43, 1–24.
Chen, Y.D., Pearson, N.J., O'Reilly, S.Y., Griffin, W.L., 1991. Applications of olivine-orthopyroxene-spinel oxygen geothermometers to the redox state of the upper mantle. Journal of Petrology, Orogenic lherzolites and mantle processes 291–306 Special Volume.
Christie, D.M., Carmichael, I.S.E., Langmuir, C.H., 1986. Oxidation states of mid-oceanic ridge basalt glasses. Earth and Planetary Science Letters 79, 397–411.
Daniels, L.R.M., Gurney, J.J., 1991. Oxygen fugacity constraints on the southern African lithosphere. Contributions to Mineralogy and Petrology 108, 154–161.
DeHoog, J.C.M., Hattori, K.H., Hoblitt, R.P., 2004. Oxidized sulfur-rich mafic magma at Mount Pinatubo, Philippines. Contributions to Mineralogy and Petrology 146, 750–761.
Dick, J.J.B., Bullen, T., 1984. Chromian spinel as a petrogenetic indicator in abyssal and alpine-type peridotites and spatially associated lavas. Contributions to Mineralogy and Petrology 86, 54–76.
D'Orazio, M., Agostini, S., Mazzarini, F., Innocenti, F., Manetti, P., Haller, M.J., Lahsen, A., 2000. The Pali Aike Volcanic Field, Patagonia: slab-window magmatism near the tip of South America. Tectonophysics 321, 407–427.
Frost, B.R., Lindsley, D.H., Andersen, D.J., 1988. Fe–Ti oxide-silicate equilibria: assemblages with fayalitic olivine. The American Mineralogist 73, 727–740.
Gorring, M.L., Kays, S.M., Zeitler, P.K., Ramos, V.A., Rubiolo, D., Fernandez, M.I., Panza, J.L., 1997. Neogene Patagonian plateau lavas: continental magmas associated with ridge collision at the Chile Triple Junction. Tectonics 16, 1–17.
Haschke, M., Sobel, E.R., Blisniuk, P., Strecker, M.R., Warkus, F., 2006. Continental response to active ridge subduction. Geophysical Research Letters, 33, L15315, doi:10.1029/2006GL025972.
Hattori, K.H., Keith, J.D., 2001. Contribution of mafic melt for porphyry deposits; evidence from Pinatubo and Bingham. Mineralium Deposita 36, 799–806.
Hattori, K.H., Guillot, S., 2007. Geochemical character of serpentinites associated with high- to ultrahigh-pressure metamorphic rocks in the Alps, Cuba and the Himalayas: recycling of elements in subduction zones. Geochemistry, Geophysics, and Geosystems (G3), doi:10.1029/2007GC001594.
Herzberg, C., 1999. Formation of cratonic mantle as plume residues and cumulates. In: Fei, Y., Bertka, C., Mysen, B.O. (Eds.), Mantle Petrology: Field Observations and High Pressure Experimentation. Geochemical Society Special Publication, vol. 6, pp. 241–257.
Ionov, D.A., Wood, B.J., 1992. The oxidation state of subcontinental mantle: oxygen thermobarometry of mantle xenoliths from Central Asia. Contributions to Mineralogy and Petrology 111, 179–193.

Ionov, D.A., Ashchepkov, I.V., Stosch, H.-G., Witt-Eickschen, G., Seck, H.A., 1993. Garnet peridotite xenoliths from the Vitim volcanic field, Baikal region: the nature of the garnet-spinel peridotite transition zone in the continental mantle. Journal of Petrology 34, 1141–1175.

Kay, S.M., Ramos, V.A., Mpodozis, C., Sruoga, P., 1989. Late Paleozoic to Jurassic silicic magmatism at the Gondwanaland margin: analogy to the Middle Proterozoic in North America? Geology 17, 324–328.

Kennedy, C.S., Kennedy, G.C., 1976. The equilibrium boundary between graphite and diamond. Journal of Geophysical Research 81, 2467–2470.

Kelemen, P.B., Hart, S.R., Bernstein, S., 1998. Silica enrichment in the continental upper mantle via melt/rock reaction. Earth and Planetary Science Letters 164, 387–406.

Kempton, P.D., Lopez-Escobar, L., Hawkesworth, C.J., Pearson, D.G., Ware, A.J., 1999a. Spinel±garnet lherzolite xenoliths from Pali Aike: Part 1. Petrology, mineral chemistry and geothermobarometry. In: Gurney, J.J., Gurney, J.L., Pascoe, M.D., Richardson, S.H. (Eds.), The J.B., Dawson Volume. Proceedings of the International Kimberlite Conference 7, vol. 1, pp. 403–414.

Kempton, P.D., Hawkesworth, C.J., Lopez-Escobar, L., Pearson, D.G., Ware, A.J., 1999b. Spinel±garnet lherzolite xenoliths from Pali Aike: Part 2. Trace element and isotopic evidence bearing on the evolution of lithospheric mantle beneath southern Patagonia. In: Gurney, J.J., Gurney, J.L., Pascoe, M.D., Richardson, S.H. (Eds.), The J.B., Dawson Volume. Proceedings of the International Kimberlite Conference 7, vol. 1, pp. 415–428.

McCammon, C., Kopylova, M.G., 2004. A redox profile of the slave mantle and oxygen fugacity control in the cratonic mantle. Contributions to Mineralogy and Petrology 148, 55–68.

McCammon, C.A., Griffin, W.L., Shee, S.R., O, 'Neill, H.St.C., 2001. Oxidation during metasomatism in ultramafic xenoliths from the Wesselton kimberlite, South Africa: implications from the survival of diamond. Contributions to Mineralogy and Petrology 141, 287–296.

McCanta, M.C., Dyar, M.D., Rutherford, M.J., Delaney, J.S., 2004. Iron partitioning between basaltic melts and clinopyroxene as a function of oxygen fugacity. The American Mineralogist 89, 1685–1693.

McDonough, W.F., Sun, S.S., 1995. The composition of the Earth. Chemical Geology 120, 223–253.

Mercier, J.C., 1980. Single-pyroxene thermobarometry. Tectonophysics 70, 1–37.

Michael, P.J., Bonatti, E., 1985. Peridotite composition from the North Atlantic: regional and tectonic variations and implications for partial melting. Earth and Planetary Science Letters 73, 91–104.

Mungall, J.E., 2002. Roasting the mantle: slab melting and the genesis of major Au and Au-rich Cu deposits. Geology 30, 915–918.

Nell, J., Wood, B.J., 1991. High-temperature electrical measurements and thermodynamic properties of Fe_3O_4–$FeCr_2O_4$–$MgCr_2O_4$–$FeAl_2O_4$ spinels. The American Mineralogist 76, 406–426.

Nickel, K.G., Green, D.H., 1985. Empirical geothermobarometry for garnet peridotites and implications for the nature of the lithosphere, kimberlites and diamonds. Earth and Planetary Science Letters 73, 158–170.

Niu, Y.L., O'Hara, M.J., 2003. The origin of ocean island basalts (OIB): a new perspective from petrology, geochemistry and mineral physics considerations. Journal of Geophysical Research 108 (B4), 2209, doi:10.1029/2002JB002048.

Niu, Y.L., 2004. Bulk-rock major and trace element compositions of abyssal peridotites: implications for mantle melting, melt extraction and post-melting processes beneath mid-ocean ridges. Journal of Petrology 45, 2423–2458.

Obata, M., Morten, L., 1987. Transformation of spinel lherzolite to garnet lherzolite in ultramafic lenses of the Austridic crystalline complex, northern Italy. Journal of Petrology 28, 599–623.

O'Neill, H.St.C., Wall, V.J., 1987. The olivine-orthopyroxene-spinel oxygen barometer, the nickel precipitation curve, and the oxygen fugacity of the Earth's upper mantle. Journal of Petrology 28, 1169–1191.

Pankhurst, R.J., Rapela, C.W., Loske, W.P., Fanning, C.M., Márquez, M., 2003. Chronological study of the pre-Permian basement rocks of southern Patagonia. Journal of South American Earth Sciences 16, 27–44.

Pankhurst, R.J., Rapela, C.W., Fanning, C.M., Márquez, M., 2006. Gondwanide continental collision and the origin of Patagonia. Earth-Science Reviews 76, 235–257.

Parkinson, I.J., Pearce, J.A., 1998. Peridotites from the Izu-Bonin-Mariana Forearc (ODP Leg 125): evidence for mantle melting and melt-mantle interaction in a supra-subduction zone setting. Journal of Petrology 39, 1577–1608.

Parkinson, I.J., Arculus, R.J., 1999. The redox state of subduction zones: insights from arc-peridotites. Chemical Geology 160, 409–423.

Parkinson, I.J., Arculus, R.J., Eggins, S.M., 2003. Peridotite xenoliths from Grenada, Lesser Antilles Island arc. Contributions to Mineralogy and Petrology 146, 241–262.

Parman, S.W., Grove, T.L., Dann, J.C., del Wit, M.J., 2004. A subduction origin for komatiites and cratonic lithospheric mantle. South African Journal of Geology 107, 107–118.

Qi, Q., Taylor, L.A., Zhou, X.M., 1995. Petrology and geochemistry of mantle peridotite xenoliths from SE China. Journal of Petrology 36, 55–79.

Ramos, V.A., 1986. Discussion of "Tectonostratigraphy, as applied to analysis of South African Phanerozoic basins" by H. de la R. Winter. Transactions of the Geological Society of South Africa 89, 427–429.

Ramos, V.A., 1989. Foodhills structures in Northern Magallanes Basin, Argentina. American Association of Petrleum Geologists Bulletin 73, 887–903.

Rapalini, A.E., 2005. The accretionary history of southern South America from the latest Proterozoic to the late Paleozoic: some palaeomagnetic constraints. Geological Society of London Special Publication 246, 305–328.

Schilling, M.E., Carlson, R.W., Conceicão, R.V., Dantas, C., Bertotto, G.W., Koester, E., 2008. Re–Os isotopic constraints on subcontinental lithospheric mantle evolution of southern South America. Earth and Planetary Science Letters 268 (1–2), 89–101.

Selverstone, M.A., Stern, C.R., 1983. Petrochemistry and recrystallization history of granulite xenoliths from the Pali Aike volcanic field, Chile. The American Mineralogist 68, 1102–1112.

Söllner, F., Miller, H., Hervé, M., 2000. An Early Cambrian granodiorite age from the pre-Andean basement of Tierra del Fuego (Chile): the missing link between South America and Antarctica? Journal of South American Earth Sciences 13, 163–177.

Stern, C.R., Kilian, R., 1996. Role of the subducted slab, mantle wedge and continental crust in the generation of adakites from the Andean Austral Volcanic zone. Contributions to Mineralogy and Petrology 123, 263–281.

Stern, C.R., Kilian, R., Olker, B., Hauri, E.H., Kyser, T.K., 1999. Evidence from mantle xenoliths for relatively thin (<100 km) continental lithosphere below the Phanerozoic crust of southernmost South America. Lithos 48, 217–235.

Von Gonsen, W., 2002. Polyphase structural evolution in the northeastern segment of the North Patagonian Massif (southern Argentina). Journal of South American Earth Sciences 15, 591–623.

Von Seckendorff, V., O'Neill, H.S.C., 1993. An experimental study of Fe–Mg partition between olivine and orthopyroxene at 1173, 1273 and 1423 K and 1.6 GPa. Contributions to Mineralogy and Petrology 113, 196–207.

Wang, J., Hattori, K.H., Kilian, R., Stern, C.R., 2007. Metasomatism of sub-arc mantle peridotites below southernmost South America reduction of fO_2 by slab-melt. Contributions to Mineralogy and Petrology 153, 607–624.

Wells, P.R.A., 1977. Pyroxene thermometry in simple and complex systems. Contributions to Mineralogy and Petrology 62, 119–139.

Wood, B.J., 1990. An experimental test of the spinel peridotite oxygen barometer. Journal of Geophysical Research 97, 15845–15851.

Wood, B.J., Virgo, D., 1989. Upper mantle oxidation state: ferric iron content of lherzolite spinels by 57Fe Mössbauer spectroscopy and resultant oxygen fugacities. Geochimica et Cosmochimica Acta 53, 1277–1291.

Woodland, A.B., Koch, M., 2003. Variation in oxygen fugacity with depth in the upper mantle beneath the Kaapvaal craton, southern Africa. Earth and Planetary Science Letters 214, 295–310.

Woodland, A.B., Kornprobst, J., Wood, B.J., 1992. Oxygen thermobarometry of orogenic lherzolite massifs. Journal of Petrology 33, 203–230.